Eur. Phys. J. Special Topics **224**, 261–276 (2015)

DOI: 10.1140/epjst/e2015-02358-2

THE EUROPEAN PHYSICAL JOURNAL SPECIAL TOPICS

Regular Article

Solutal Marangoni convection in a Hele–Shaw geometry: Impact of orientation and gap width

T. Köllner[1,a], K. Schwarzenberger[2], K. Eckert[2], and T. Boeck[1]

[1] Institute of Thermodynamics and Fluid Mechanics, TU Ilmenau, PO Box 100565, 98684 Ilmenau, Germany
[2] Institute of Fluid Mechanics, Chair of Magnetofluiddynamics, Measuring and Automation Technology, TU Dresden, 01062 Dresden, Germany

Received 31 July 2014 / Received in final form 16 February 2015
Published online 8 April 2015

Abstract. We study Marangoni roll cell convection in a ternary mass transfer system composed of cyclohexanol, water and butanol (transferred species) placed in a Hele-Shaw cell. A detailed comparison of experimental and numerical results is carried out for four different cases including horizontal and vertical orientation as well as small and large gap width of the Hele-Shaw cell. The numerical simulations are based on a common gap-averaged model. For the small gap width, the numerical results qualitatively represent the experimental results. However, by comparison with the experiments, the time evolution in the simulation appears generally retarded. The results show that three-dimensional flow effects have to be expected in particular for a horizontal orientation and a large gap width.

1 Introduction

In a Hele-Shaw setup, the fluids are enclosed between two parallel plates that are sufficiently close together such that the fluid motion becomes mainly two-dimensional. The Hele-Shaw (HS) cell is a versatile experimental and numerical configuration in chemical engineering studies of biphasic systems [1–8], e.g. to investigate transport processes at liquid interfaces. This setup provides simplified access to the vertical structure of quantities recorded by optical methods such as shadow-graphy, interferometry and particle image velocimetry. By varying the orientation of the HS cell, it is possible to reveal information about the influence of gravity [9–12].

Also from the viewpoint of theoretical modeling, the HS setup is advantageous since it may be described by a two-dimensional (2D) model based on gap-averaged equations [7], which significantly saves computational cost compared to full three-dimensional (3D) simulations. A similar motivation underlies studies that assume a pure 2D model without the influence of wall friction [13,14]. Despite this interest, a detailed one-to-one comparison of experimental observations to numerical simulations of solutal Marangoni convection in the HS setup is still lacking.

[a] e-mail: thomas.koellner@tu-ilmenau.de

The aim of the present work is to study such a Marangoni convection in the HS geometry for the chemical system: cyclohexanol with dissolved butanol superposed to an aqueous layer. The surface-tension and density lowering butanol diffuses to the aqueous layer. Since the aqueous layer has lower kinematic viscosity and higher solute diffusivity, this configuration is unstable with respect to stationary Marangoni instability as predicted by the linear stability analysis of Sternling & Scriven [15]. The mechanism that drives the flow is as follows: Consider a location at the interface with a positive variation of butanol. Inevitably, interfacial forces by lowered interfacial tension will create a flow that spreads butanol tangentially to the interface, away from this initial variation. The ensuing flow from the bulk carries fluid which is poor in butanol (from the lower layer) and rich in butanol (upper layer) to the interface. This transport increases the interfacial concentration due to lower diffusivity in the upper, butanol-rich layer. Hence, interfacial tension gradients are amplified and Marangoni convection is established.

Recently, we investigated solutal Marangoni convection in this system when placed in a 3D setup [16]. The *horizontal* structure of the simulated hierarchical Marangoni roll cells compared well to our own and to independent experiments [17]. Now, by using a HS cell instead of the 3D setup of [16], we are able to experimentally observe the *vertical* structure of the emerging Marangoni roll cells. Four cases are considered using 0.5 mm and 1 mm gap width and a vertical and horizontal orientation of the HS cell. On this basis, we discuss the applicability of the 2D gap-averaged model by comparing structures and measured heights of Marangoni cells from simulations and experiments.

This paper is divided into four main sections. Section 2 details the experimental procedure and the theoretical model. The experimental and numerical results are consecutively presented in Sect. 3 for the four different cases. A rough analytic estimation is given in Sect. 4 for the parasitic density convection in the horizontally oriented HS cell. A concluding discussion in Sect. 5 interprets deviations of the experiment from the model.

2 Methods

2.1 Experiments

We consider mass transfer of 1-butanol from an upper cyclohexanol-rich layer (2) to a lower water-rich layer (1). As a first step, the binary phases of cyclohexanol and water are equilibrated by mutual saturation, which reduces effects from phase changes and multi-component diffusion. After phase separation, 7.5 vol% butanol is added to the cyclohexanol-rich phase which corresponds to a molar concentration of $c_0 = 0.82$ mol/l according to the reference experiment in [16].

To obtain the HS configuration, the liquid-liquid system is placed in a narrow gap between two glass plates. Figure 1 sketches the experimental HS setup (a) and the computational domain (b), which is drawn as a gray inset in (a) for comparison. A spacer made of polytetrafluoroethylene (PTFE) foil, whose inner contour is shown as a dashed line in Fig. 1a, acts as a container for the liquids. The gap width 2ϵ, see Fig. 1b, is set by the thickness of the foil: we use a thickness of 0.5 mm and 1 mm. The width of the interface, marked by a dotted line and horizontal arrow in Fig. 1a, amounts to 30 mm.

For the analysis of the experimental data (Sect. 3) only the central 20 mm of the interface are considered. This is done to disregard boundary effects that arise in the vicinity of the pinning edges and near the outflow channels, cf. Fig. 1a. In the simulations, we use these 20 mm as the horizontal domain size L_x, see Fig. 1b.

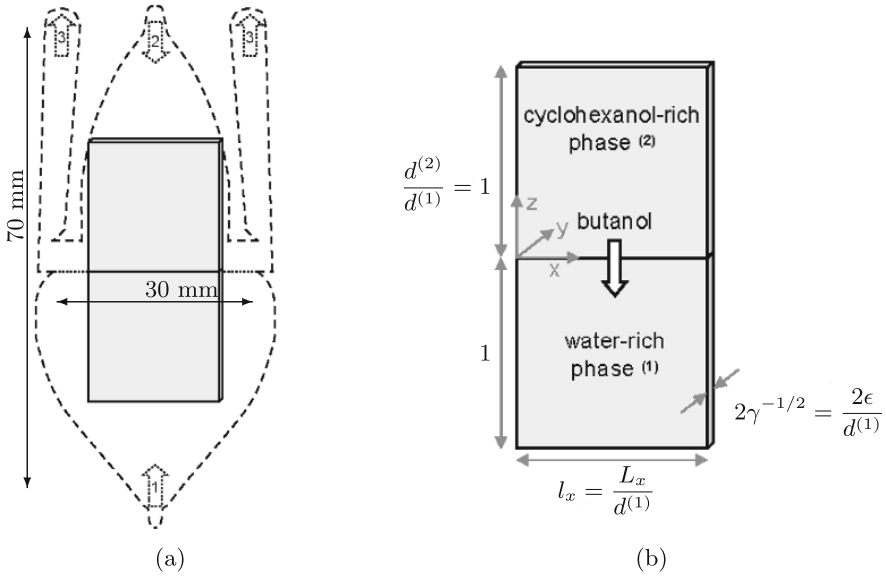

(a) (b)

Fig. 1. Hele-Shaw (HS) geometry: as experimental setup (a) according to [18] with gray inset of numerical domain; detailed numerical domain (b) in dimensionless lengths (scaled by lower layer height $d^{(1)} = 20\,\text{mm}$).

According to the geometry employed in [16], layer heights are set to $d^{(1)} = d^{(2)} = 20\,\text{mm}$. In the experimental HS cell, the height of the liquid layers (approx. 35 mm) is larger. However, since Marangoni convection is restricted to a small zone near the interface, this difference is expected to be negligible.

The shape of the PTFE foil was optimized to provide a robust filling procedure for different two-phase systems [18]. The numbered arrows in Fig. 1a mark relevant stages of this filling procedure. In step 1, the aqueous phase is injected in the lower half of the container until its surface is pinned at the lateral edges of the PTFE foil. During the filling of the organic phase in the second half of the container (step 2), the HS cell has to be placed in a horizontal position, i.e. the acceleration due to gravity is $\mathbf{g} = g\mathbf{e}_y$ (Fig. 1b). When the organic phase contacts the aqueous surface, the interface (dotted line) is established quickly via spreading of the organic phase. Finally in step 3, the exhaust channels are filled to avoid side effects of the air-liquid interface. The duration of the last step involves a compromise between an uncontrolled mass transfer during slow filling and an increased interfacial deformation for rapid filling. This rather delicate experimental procedure is due to the interfacial tension of the system cyclohexanol/water ($\sigma_{ref} = 3.4\times10^{-3}$ N/m), which is low when compared to the alkane/water systems mostly used in this HS cell design [2,3,9–11,18].

To vary gravity influence, the HS cell can either remain horizontally ($\mathbf{g} = g\mathbf{e}_y$) or it is tilted to a vertical position ($\mathbf{g} = -g\mathbf{e}_z$, Fig. 1) immediately after filling.

The concave meniscus[1] (viewed from the aqueous layer) that is formed across the plates is characterized by its height $\tilde{\omega}$ given by the wall-parallel distance of the triple line to the apex (the lowest point) of the meniscus. It was measured at both plate

[1] The interface position might be described by a height function $z = \xi(x, y)$. In these terms, "concave" means $\partial_y^2 \xi(x, y) \geq 0$ and the measured meniscus height (being effectively constant over x) is $\tilde{\omega} = \max_y(\xi(x, y)) - \min_y(\xi(x, y))$, cf. Fig. 9. In our theoretical model $\xi(x, y) = 0$.

distances of $2\epsilon = 0.5\,\text{mm}$ (1 mm) and is $\tilde{\omega}$=0.094 mm (0.180 mm). The corresponding contact angle (with respect to the aqueous layer) is estimated to $\theta \approx 50°$. This calculation assumes a circular interface as the corresponding Bond number is below unity.

Pattern evolution in the course of the experiment is visualized by a shadowgraph optics operating in transmission (TSO, Germany). Additionally, particle image velocimetry (PIV) measurements are conducted in the vertically oriented HS cell for two different gap widths (0.5 and 1 mm). In this process, the whole volume is illuminated by a cold light source and the optics recording the light scattered by tracer particles is focused on the center plane. Solvent-resistant melamine resin particles (particle size 3.97 μm, density 1.51 g/cm^3; microParticles, Germany) serve as tracers since buoyantly neutral polystyrene particles were found to influence interfacial dynamics. For the given material parameters of the particles and fluids, and the characteristics of the convection, the Stokes number is estimated to 2.1×10^{-9}, thus tracing accuracy with respect to inertial effects is high. However, PIV records are solely evaluated in the upper organic phase since sedimentation and agglomeration of particles are significant in the aqueous phase. These undesired effects are strongly suppressed in the cyclohexanol-rich phase by its high viscosity. Furthermore, PIV, when using high optical magnification, is sensitive to external vibrations. Hence, only PIV images with zero velocity far from the interface are considered.

2.2 Hele-Shaw model

The flow in the HS setup is simulated by a common gap-averaged hydrodynamic model [6,19,20], which assumes a parabolic flow profile, no solute variation along the y-direction and a plane undeformable interface. The system is assumed isothermal. Interfacial tension (σ) and density ($\rho^{(i)}$) in layer $^{(i)}$ depend linearly on dimensional solute (i.e. butanol) concentration ($\tilde{c}^{(i)}$),

$$\rho^{(i)} = \rho^{(i)}_{ref} + \rho^{(i)}_{ref}\beta^{(i)}_c\tilde{c}^{(i)}, \tag{1}$$

$$\sigma = \sigma_{ref} + \sigma_{ref}\alpha_c\tilde{c}^{(1)}, \tag{2}$$

while the other material properties are constant in each phase. This dependence is quantified by the solutal expansion coefficients ($\beta^{(i)}_c$) and the coefficient of interfacial tension change (α_c) given in Table 1 for the experimental situation. A comprehensive description of the general three-dimensional two-layer flow model can be found in [26].

The problem is nondimensionalized with viscous units, where the unit of length is the lower layer height $d^{(1)} = 20\,\text{mm}$, unit of time is $(d^{(1)})^2/\nu^{(1)} = 333\,\text{s}$, unit of pressure is $\mu^{(1)}\nu^{(1)}/(d^{(1)})^2 = 3.59 \times 10^{-6}$ N/m^2 and unit of solute concentration is $c_0 = 0.82$ mol/l. The ratio of squared layer height to half plate distance is $\gamma = \frac{(d^{(1)})^2}{\epsilon^2} = 6400$ ($2\epsilon = 0.5\,\text{mm}$), 1600 ($2\epsilon = 1\,\text{mm}$), cf. Fig. 1b. By this definition, the nondimensional plate distance is $2\gamma^{-1/2} = 0.025$ (thin), 0.05 (thick). As introduced in Sect. 2.1 and illustrated by Fig. 1b, the fluid is located in a box $(x, y, z) \in [0, l_x] \times [-\gamma^{-1/2}, \gamma^{-1/2}] \times [-1, 1]$ composed of layer$^{(1)}$ for $z < 0$ and layer$^{(2)}$ for $z > 0$.

For the modeling, we follow the formulation by averaging over the gap. This simplifies the three-dimensional governing equations that have been successfully applied to this system [16]. Specifically, the following two assumptions are applied. First, the nondimensional velocity field $\mathbf{u}^{(i)}(x, y, z, t)$ in

Table 1. Basic parameters for HS simulation in the cyclohexanol + 7.5 vol% butanol → water system. The acceleration due to gravity is $g = 9.81\,\mathrm{m/s^2}$. Both layer heights are set to $d^{(1)} = d^{(2)} = 20\,\mathrm{mm}$.

Description	Symbol	Value
mass density (1)	$\rho_{ref}^{(1)}$	$997\,\mathrm{kgm^{-3}}$
mass density (2)	$\rho_{ref}^{(2)}$	$955\,\mathrm{kgm^{-3}}$
kinematic viscosity (1)	$\nu^{(1)}$	$1.2 \times 10^{-6}\,\mathrm{m^2\,s^{-1}}$
kinematic viscosity (2)	$\nu^{(2)}$	$20 \times 10^{-6}\,\mathrm{m^2\,s^{-1}}$
diffusivity butanol (1)	$D^{(1)}$	$5 \times 10^{-10}\,\mathrm{m^2\,s^{-1}}$
diffusivity butanol (2)	$D^{(2)}$	$7 \times 10^{-11}\,\mathrm{m^2\,s^{-1}}$
interfacial tension of the binary system	σ_{ref}	$3.4 \times 10^{-3}\,\mathrm{Nm^{-1}}$
change in interfacial tension via $c^{(1)}$	$\sigma_{ref}\alpha_c$	$-8.77 \times 10^{-3}\,\mathrm{Nm^{-1}/(mol\,l^{-1})}$
solutal expansion coefficient (1)	$\beta_c^{(1)}$	$-0.0172\,\mathrm{l\,mol^{-1}}$
solutal expansion coefficient (2)	$\beta_c^{(2)}$	$-0.0128\,\mathrm{l\,mol^{-1}}$
Schmidt number aqueous phase	$Sc^{(1)} = \dfrac{\nu^{(1)}}{D^{(1)}}$	2400
Marangoni number	$Ma = \dfrac{c_0\alpha_c\sigma_{ref}d^{(1)}}{\rho^{(1)}\nu^{(1)}D^{(1)}}$	-2.4×10^8
Grashof number	$G = \dfrac{c_0\beta_c^{(1)}g(d^{(1)})^3}{(\nu^{(1)})^2}$	-7.67×10^5(vertical) or 0 (horizontal)
partition coefficient	$H = c_{eq}^{(2)}/c_{eq}^{(1)}$	31
density ratio	$\rho = \dfrac{\rho_{ref}^{(2)}}{\rho_{ref}^{(1)}}$	0.96
kinematic viscosity ratio	$\nu = \dfrac{\nu^{(2)}}{\nu^{(1)}}$	16.7
diffusivity ratio	$D = \dfrac{D^{(2)}}{D^{(1)}}$	0.14
ratio of expansion coefficients	$\beta = \dfrac{\beta_c^{(2)}}{\beta_c^{(1)}}$	0.75
layer height to thickness squared	$\gamma = \dfrac{(d^{(1)})^2}{\epsilon^2}$	6400(thin), 1600(thick)

layer$^{(i)}$ is assumed two-dimensional ($u_y^{(i)} = 0$) with a parabolic dependence on y, i.e.

$$\mathbf{u}^{(i)}(x,y,z) = \frac{3}{2}(1-y^2\gamma)(v_x^{(i)}(x,z)\mathbf{e}_x + v_z^{(i)}(x,z)\mathbf{e}_z). \tag{3}$$

In what follows, we are concerned with velocity fields that are gap-averaged over y and denoted by $\mathbf{v}^{(i)}(x,z,t) = \langle \mathbf{u}^{(i)} \rangle_y$. The second assumption is that solute concentration is constant across the gap, i.e. it does not depend on the y-coordinate: $c^{(i)} = c^{(i)}(x,z,t)$.

With these assumptions the 3D Navier-Stokes-Boussinesq equations and advection-diffusion equations for the solute simplify to the two-dimensional HS model, note that we have used viscous units for nondimensionalization):

$$\partial_t \mathbf{v}^{(1)} = -\frac{6}{5}\mathbf{v}^{(1)} \cdot \nabla \mathbf{v}^{(1)} - \nabla p_d^{(1)} + \Delta \mathbf{v}^{(1)} - c^{(1)} G \mathbf{e}_z - 3\gamma \mathbf{v}^{(1)}, \tag{4}$$

$$\partial_t \mathbf{v}^{(2)} = -\frac{6}{5}\mathbf{v}^{(2)} \cdot \nabla \mathbf{v}^{(2)} - \frac{1}{\rho}\nabla p_d^{(2)} + \nu \Delta \mathbf{v}^{(2)} - c^{(2)} G \beta \mathbf{e}_z - 3\gamma\nu \mathbf{v}^{(2)}, \tag{5}$$

$$\nabla \cdot \mathbf{v}^{(1)} = 0, \quad \nabla \cdot \mathbf{v}^{(2)} = 0, \tag{6}$$

$$\partial_t c^{(1)} = -\mathbf{v}^{(1)} \cdot \nabla c^{(1)} + \frac{1}{Sc^{(1)}} \Delta c^{(1)}, \quad \partial_t c^{(2)} = -\mathbf{v}^{(2)} \cdot \nabla c^{(2)} + \frac{D}{Sc^{(1)}} \Delta c^{(2)}. \tag{7}$$

The definition of the parameters appearing in the equations above and their values are summarized in Table 1. Bottom ($z = -1$) and top ($z = 1$) boundaries are considered as impermeable solid walls

$$\partial_z c^{(2)} = v_z^{(2)} = v_x^{(2)} = 0 \quad \text{for } z = 1, \quad \partial_z c^{(1)} = v_z^{(1)} = v_x^{(1)} = 0 \quad \text{for } z = -1. \tag{8}$$

At the plane interface ($z = 0$), the solute mass fluxes and velocities are continuous, bulk concentrations are in equilibrium and tangential stresses are related to interfacial tension gradients:

$$\partial_z c^{(1)} = D \partial_z c^{(2)}, \quad v_x^{(1)} = v_x^{(2)}, \quad v_z^{(1)} = v_z^{(2)} = 0, \tag{9}$$

$$H c^{(1)} = c^{(2)}, \quad \frac{Ma}{Sc^{(1)}} \partial_x c^{(1)} = -\mu \partial_z v_x^{(2)} + \partial_z v_x^{(1)}. \tag{10}$$

The x-direction is periodic, so velocity $\mathbf{v}^{(i)}$ and concentrations $c^{(i)}$ obey $f(x+l_x, z, t) = f(x, z, t)$, where the horizontal length is $l_x = 1$. Initially, butanol is only present in layer$^{(2)}$, i.e. $c^{(1)}(x, z, t = 0) = 0$, $c^{(2)}(x, z, t = 0) = 1$. Furthermore, velocity is zero except for a small amount of noise added to the vertical velocity in order to trigger Marangoni instability as described in [16].

The numerical method rests on a pseudo-spectral algorithm using a Fourier expansion in x with N_x modes and a Chebychev expansion in z with polynomial degree $N_z^{(i)}$. The resolution is $N_x = 2048$ and $N_z^{(1)} = N_z^{(2)} = 256$. The mesh points are non-equidistant in z-direction, i.e. clustered near the interface where a better resolution is required compared to the bulk. The present code has been used in former studies [16,21] where details can be found. The additional damping with prefactor 3γ in Eq. (4) is well known from Darcy's law. It is treated implicitly in time. Our implementation was validated by simulating a case presented in [20] for pure density convection (results not shown here). Reasonable agreement was found regarding the pattern characteristics and the evolution of length scales.

2.3 Discussion of the Hele-Shaw model

After the introduction of our theoretical model, we give a short review on the modeling of flows in a HS-cell and show the problems which are inherent in our assumptions. Generally, the gap-averaged model is clearly restricted to a physical situation where viscous and diffusive perturbations equilibrate sufficiently fast across the gap on a comparable time scale. Apart from the deviations caused by 3D flow effects and interfacial deformations (as discussed in Sect. 5), which mainly have an effect in

the vicinity of the interface, the bulk flow in the Hele-Shaw model might as well be a source of discrepancies between experiment and simulation. Former works have proposed certain model corrections for the bulk. However, they have typically focused either on the momentum or on the species balance but not on both.

Momentum transport

The assumption of a parabolic profile in the Navier-Stokes equation may be violated due to gradients in density, viscosity, or geometrical effects. Ruyer-Quil [32] derived a gap-averaged equation as a first order correction to the parabolic profile. He found inertial terms with other prefactors: $\frac{6}{5}\partial_t \mathbf{v}^{(1)} + \frac{54}{35}\mathbf{v}^{(1)} \cdot \nabla \mathbf{v}^{(1)} = -\nabla p - 3\gamma \mathbf{v}^{(1)}$. Another approach was pursued by Zeng et al. [35], who started with the steady Stokes equation in three dimensions and solved different examples including a density-driven case and a case with viscosity gradients. It is concluded there that the viscous term (the so-called Brinkmann correction) should carry a prefactor $\beta = 12/\pi^2$, which yields $0 = -\nabla p - 3\gamma \mathbf{v}^{(1)} + \beta \Delta \mathbf{v}^{(1)}$. A later work [30] adopted this approach with modifications of β.

In the Stokes limit for interfacial-tension driven flows, however, Boos et al. [19] and Gallaire et al. [34] discussed and showed the good quality of the parabolic assumption, i.e. $\beta = 1$. By examining the Rayleigh-Taylor instability, Martin et al. [33] compared Ruyer-Quil's model (with additional second order correction $6/5\Delta \mathbf{v}^{(1)}$) to the one we introduced, i.e. Eqs. (4) and (5). In summary, they recommended the model we are using.

As a final remark on the momentum balance, let us note that when inertia is small compared to viscous forces (Reynolds number $Re \ll 1$), the Brinkman equation [19] can be used instead of Eqs. (4) and (5), i.e. the terms $\partial_t \mathbf{v}^{(i)} + \frac{6}{5}\mathbf{v}^{(i)} \cdot \nabla \mathbf{v}^{(i)}$ are omitted in these equations. Actually, by estimating Re a posteriori from the typical velocity and size of the convection cells in Fig. 7, it can be shown that $Re \ll 1$ applies for our system. Consequently, neglecting inertial terms in the momentum balance is possible. However, for other Marangoni-unstable systems this may not be the case. Therefore we adopt the more general model.

Species transport

The second assumption is the quasi instantaneous equilibration of the concentration field across the gap. It demands that the diffusion time $\tau_d = \epsilon^2/D^{(i)}$ is much lower than the characteristic time for advection $\tau_a = \epsilon/\tilde{U}$. The "cross-gap" Péclet number $Pe = \tau_d/\tau_a = \tilde{U}\epsilon/D^{(i)}$ is evaluated with the experimentally measured velocity $\tilde{U} \approx 10\,\mu$m/s (see Fig. 7). In the case of the thin cell ($\epsilon = 0.25$ mm), the Péclet number in the lower (upper) layer is Pe= 5 (35.7) and for the thicker cell ($\epsilon = 0.5$ mm) it is Pe = 10 (71.4).

Clearly, this leads to the effect of Taylor dispersion [27], i.e. solute in the middle of the gap is transported faster than in the vicinity of the plates. Taylor and later Aris [28] showed for a simpler geometrical configuration that this process could be accounted for by a transport with the mean velocity and an additional dispersion term. Recently, the dispersion effect for *unidirectional* flows has been incorporated in density-driven flows [29,30].

For the *non-unidirectional* flows we are concerned within this study, Zimmermann *et al.* [31] proposed a model based on the analysis of Horne *et al.* [36], which Zimmerman *et al.* and Petitjeans *et al.* [37] used to study miscible displacement in the Hele-Shaw setup. To the best of our knowledge this is the most reasonable two-dimensional model that includes the effect of Taylor dispersion. Zimmermann *et al.*

cast the effect of Taylor dispersion into an anisotropic and velocity-dependent diffusivity tensor $\mathbf{D}$. The new transport equation for solute in layer $^{(i)}$ then reads (for dimensional quantities that have a nondimensional counterpart we add a tilde)

$$\partial_{\tilde{t}}\tilde{c}^{(i)} + \tilde{\mathbf{v}}^{(i)} \cdot \tilde{\nabla}\tilde{c}^{(i)} = \tilde{\nabla} \cdot (\mathbf{D}^{(i)} \cdot \tilde{\nabla}\tilde{c}^{(i)}). \tag{11}$$

The dispersion tensor is given as follows:

$$\mathbf{D}^{(i)} = D^{(i)}\mathbf{I} + \frac{2\epsilon^2}{105D^{(i)}}\tilde{\mathbf{v}}^{(i)} \otimes \tilde{\mathbf{v}}^{(i)}, \tag{12}$$

where $\mathbf{I}$ is the unity tensor. This formulation leads to an enhanced diffusion in flow direction while there is only molecular diffusion orthogonal to the flow. Since this model is just a heuristic extension of the analysis of Horne *et al.* [36], the validity of this approach is not assured, especially near the interface where the dispersion effect should increase the transport of solute in the center of the HS cell.

Nevertheless, to roughly estimate the influence of Taylor dispersion, we applied this model for the case of the thin and vertically oriented cell. The simulations with the dispersion model only *marginally* departed from our standard model without dispersion. After an inital phase (t<1) for which the dispersion model evolves faster, the difference in the cell height η (introduced in the following section) amounted to the typical variance between all simulation runs, i.e distinctly below 10% relative deviation. In view of these small differences and the weak rigorous foundation of the dispersion correction we decided to work with the formulation described in Sect. 2.2.

3 Results of Marangoni convection studies

Based on the HS model, we study butanol transport from the top$^{(2)}$ to the bottom$^{(1)}$ layer that causes Marangoni convection. We consider four cases that differ in the plate distance $2\epsilon = 0.5\,\text{mm}$ (*thin*), 1 mm (*thick*) and in the orientation of the cell, i.e. *vertical* or *horizontal*.

3.1 *Thin* and *vertically* oriented Hele-Shaw cell

The convective structures in experiment and simulation have the closest resemblance in the thin cell ($2\epsilon = 0.5\,\text{mm}$) and for vertical orientation. A sequence of experimental and corresponding numerical shadowgraph images $s(x, z)$ [22],

$$s(x, z) = (\partial_x^2 + \partial_z^2)c(x, z, t), \tag{13}$$

is given in Fig. 2. The maximum and minimum of the numerical gray scale, see Fig. 2b, is adapted to the experimental images (a) at one time and remains unchanged thereafter.

A conspicuous feature is the region of *mixed fluid* (poor in solute, i.e. butanol). It is bordered by a slightly darker rim to fluid rich in solute at the top and by the interface at the bottom. As dark colors mainly correspond to negative values $s(x, z, t) < 0$, see Eq. (13), they could be interpreted as a loss of solute (here to the mixed fluid) by molecular diffusion. The dark rim is bent to the interface at the *inflow regions*, which is illustrated by white circles with "A" mark in Figs. 2c,d, where butanol-rich fluid from the bulk flows to the interface. Apparently, the horizontal size of the roll cells (distance from inflow to inflow) is larger in experiments, but the trend for *coarsening*, i.e. a general growth of length scales in time, is seen both in experiment and

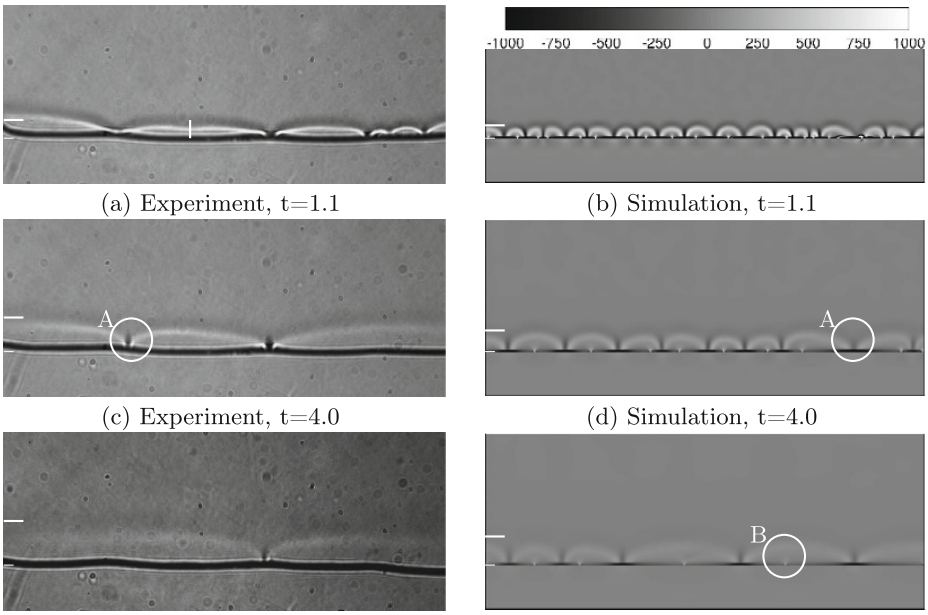

(a) Experiment, t=1.1 (b) Simulation, t=1.1

(c) Experiment, t=4.0 (d) Simulation, t=4.0

(e) Experiment, t=9.4 (f) Simulation, t=9.4

Fig. 2. *Thin, vertical HS cell*: shadowgraph images for experiment with $2\epsilon = 0.5\,\text{mm}$, corresponding to $\gamma = 6400$ in the simulation (right column). All figures show the same domain with horizontal extent of one length unit $l_x = 1$ (20 mm) and vertical extent of 0.4 length units with 0.3 in the upper phase and 0.1 in the lower phase (20 mm × 8 mm). The grayscale for simulations is fixed and given in (b). The vertical distance between the white lines illustrates the derived cell heights η, cf. Fig. 3. White circles with mark A (c), (d) illustrate what is called an inflow region, the white circle with B in (f) marks an outflow region.

simulation. Between the inflow regions, the *outflow regions* (where fluid is diverted into the bulk) are well resolved in simulations by small bright spikes, e.g. detailed in Fig. 2f by white "B" mark. In the experimental images the outflow regions are not that obvious. Moreover, the interface between both layers appears thicker in the experiment due to the deflection of light at the curved meniscus.

A quantitative comparison is carried out by measuring the roll-cell height η marked by the distance between the horizontal lines in the shadowgraph images of Fig. 2. The experimental cell height is extracted at the outflow points of the roll cells x_{out} illustrated with a vertical line in Fig. 2a. It is measured as the distance from the lower edge of the concave meniscus to the local minimum (darkest gray shade) of $s(x = x_{out}, z > 0)$ in the organic phase. This procedure is performed manually since the experimental images are perturbed by optical inhomogeneities. A mean value over all cells is plotted in Fig. 3 (black crosses) together with the standard deviation as error bars.

For the cell height data, only experiments with the least pronounced interfacial deformations (also shown in Figs. 2, 4, 5) are evaluated. These experiments required a quite slow filling of the HS cell lasting approx. 0.4 viscous time units. The starting point $t = 0$ is defined as the average between the moment of phase contact and the end of the filling procedure with a related temporal uncertainty of $t \pm 0.2$ (viscous time units).

The simulated cell height η (full lines in Fig. 3) is determined similarly but in a fully automated way: the synthetic shadowgraph distribution is averaged along the

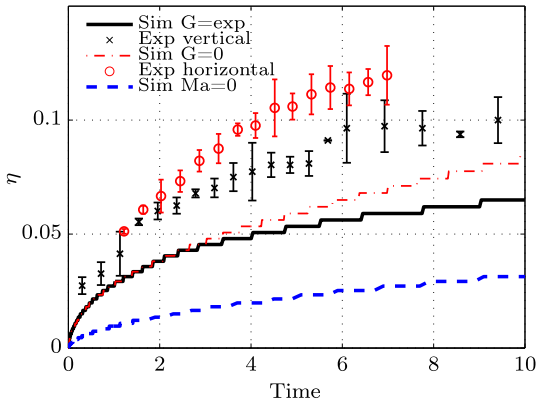

Fig. 3. *Thin HS geometry* with varied orientation: cell height η of the Marangoni cells versus time for experiment with $2\epsilon = 0.5\,\text{mm}$ and corresponding simulation with $\gamma = 6400$.

x-direction $\langle s(x,z)\rangle_x$ and searched for the local minimum with highest vertical distance to the interface, formally,

$$\eta = \max\{z : \partial_z \langle s(x,z)\rangle_x = 0\}. \tag{14}$$

As expected, the coarsening of roll cells according to Fig. 2 is also reflected in the calculated cell height (Fig. 3) for both experiment and simulation. Experimental heights exceed simulated ones by approximately 0.025 length units, which is considerable compared to the meniscus height $\omega = \tilde{\omega}/d^{(1)} = 0.0047$ or the gap size $2\gamma^{-1/2} = 0.025$. Furthermore, η was simulated for purely diffusive transport ($Ma = 0$, blue dashed line in Fig. 3). It turns out that already for the small gap size the deviations of the experimental data are of the same order of magnitude as the accelerating effect of interfacial convection in the simulations. However, it is in line with former simulations [16] that height and horizontal dimension of experimental cells increase simultaneously (readily visible in Fig. 2), since both scales are coupled by the coarsening mechanism.

3.2 *Thin* and *horizontally* oriented Hele-Shaw cell

The transport of butanol leads to a stabilizing density stratification in both phases for vertical orientation as the *mixed fluid* (adjacent to the interface) becomes denser in the upper organic and lighter in the lower aqueous phase. 3D simulations [23] proved that this density stratification retards mass transfer and cell height growth relative to zero density variation. Now this situation is studied experimentally by leaving the HS cell in a horizontal position after filling and numerically by setting the Grashof number $G = 0$.

Figures 3 and 4 show that the growth of cell height is increased when density stratification by solute transport is excluded. As for vertical orientation, the experiment appears distinctly accelerated when compared with the simulation, but the main flow structures appear identical.

3.3 *Thick* and *vertically* oriented Hele-Shaw cell

Next the impact of a doubled plate distance $2\epsilon = 1\,\text{mm}$ is studied. First notice the shadowgraph images for vertical orientation in Fig. 5: in the experimental image (a)

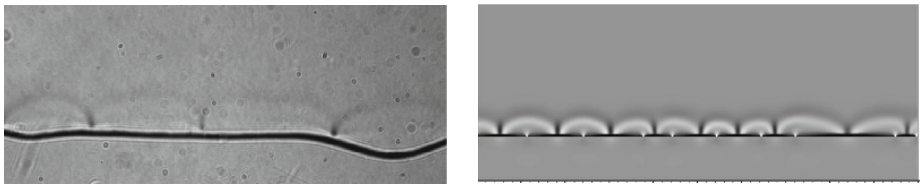

(a) Experiment horizontal (b) Simulation $G = 0$

Fig. 4. *Thin, horizontal HS cell*: shadowgraph images at t = 4.0 for (a) experiment with $2\epsilon = 0.5\,\text{mm}$ and (b) simulation with $G = 0$, $\gamma = 6400$.

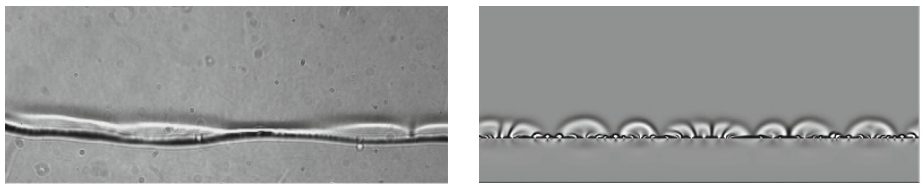

(a) Experiment (b) Simulation

Fig. 5. *Thick, vertical HS cell*: shadowgraph images at t = 1.1 for (a) experiment with $2\epsilon = 1\,\text{mm}$ and (b) simulation with $\gamma = 1600$.

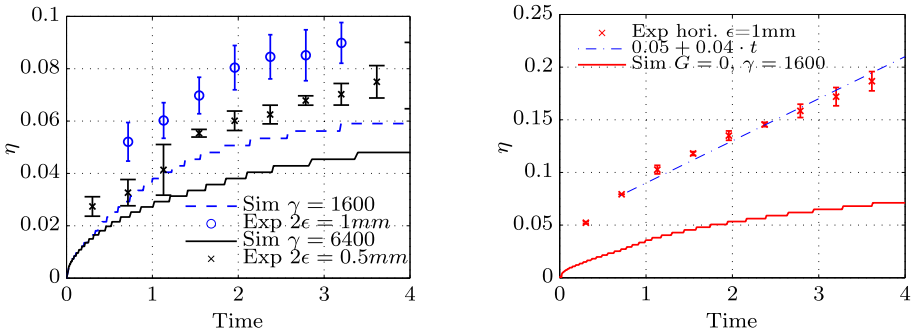

(a) Vertical orientation (b) Horizontal orientation

Fig. 6. HS cell with varied gap size and varied orientation: (a) cell height for vertical orientation and both plate distances (experiment with $2\epsilon = 0.5\,\text{mm}$, 1 mm and simulation with $\gamma = 6400$, $\gamma = 1600$); data for thin cell firstly shown in Fig. 3 is repeated for direct comparison. (b) cell height for horizontal orientation with thick gap size (experiment with $2\epsilon = 1\,\text{mm}$ and simulation with $G = 0$, $\gamma = 1600$). The dashed line is plotted to guide the eye.

the dark boundary of mixed fluid is still well visible but the clear horizontal division into individual roll cells has disappeared. A second remarkable observation is the appearance of a hierarchical pattern of small and large roll cells in the simulation, cf. Fig. 5b. This multiscale structure is a common feature of solutal Marangoni convection [16,23], which has been recently studied and explained in [16] as a *local instability* at the inflow regions of the large roll cells. In the experimental image (a) the small substructures observed in simulation are only faintly visible by a dim horizontal modulation near the interface due to the shadowing effect of the curved meniscus.

The corresponding cell height is again calculated (Fig. 6, blue circles): it is increased relative to the thin cell (black crosses again plotted for direct comparison). Remarkably, its value is of similar magnitude as the plate distance $2\gamma^{-1/2} = 0.05$

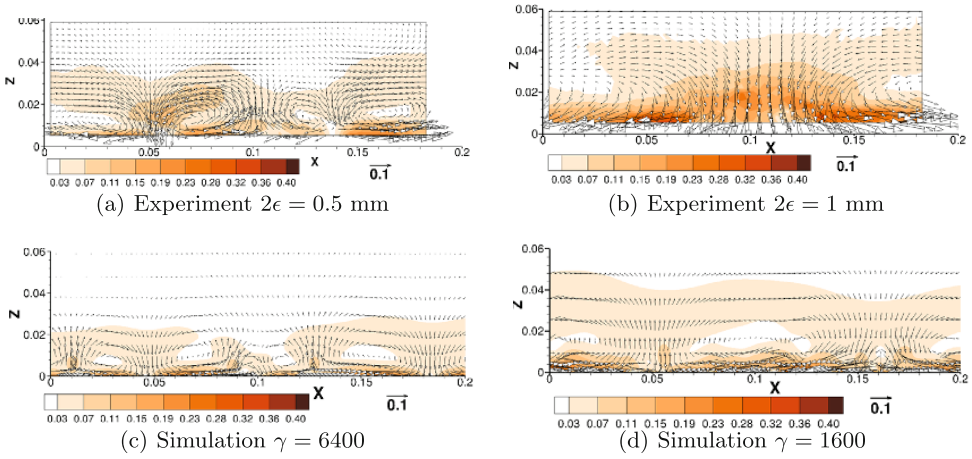

(a) Experiment $2\epsilon = 0.5$ mm (b) Experiment $2\epsilon = 1$ mm

(c) Simulation $\gamma = 6400$ (d) Simulation $\gamma = 1600$

Fig. 7. *Vertical HS cell* with varied gap size: experimental (PIV) and simulated velocity ($\mathbf{v}^{(2)}$) fields at t = 1.6. The color illustrates the amplitude of velocity. Note that the velocity scale is $\nu^{(1)}/d^{(1)} = 60$ μm/s.

(meniscus height is $\omega = \tilde{\omega}/d^{(1)} = 0.009$), i.e. three-dimensional flow effects can be expected. Likewise, the cell heights increase in the simulations for the large plate distance, see blue dashed line in Fig. 6a. However, the distinct deviations to the experimental data remain, see blue circles and blue dashed line in Fig. 6a.

Figure 7 displays the experimental (upper row) and numerical (lower row) velocity field in the top fluid layer for both plate distances and vertical orientation. In general, Fig. 7 confirms and augments the two main findings derived so far from the shadowgraph images. First, Marangoni convection in the experiments operates on larger length scales and at higher velocity but has the same flow topology as in the simulations. Second, increased plate distance leads to an intensified flow, i.e. the flow reaches further into the bulk and the inflow region has a broader horizontal extent.

3.4 *Thick* and *horizontally* oriented Hele-Shaw cell

In the case of a thick HS cell ($2\epsilon = 1$ mm, $\gamma = 1600$) with horizontal orientation ($G = 0$), the simulation shows an intensified flow in Fig. 6b and 8b, i.e. smaller substructures and increased η compared to the vertical orientation. However, the corresponding experiment differs clearly in the observed flow structures, cf. Fig. 8a: a *solute front* (see "C" mark) emerges which is almost equidistant to the interface along with a regular horizontal modulation adjacent to the interface. The solute front moves away from the interface. Its position is measured analogously to the cell height and plotted in Fig. 6b. A probable cause of the different appearances is the interference of Marangoni convection with a buoyancy-driven flow as discussed in Sect. 4.

4 Density convection in horizontal orientation

This section suggests an explanation for the solute front that is observed in the thick and horizontal cell, cf. Fig. 8a. For this, let us consider layer (2) when the HS cell is filled and mass transfer has started (see Fig. 9 for illustration): Dense mixed fluid

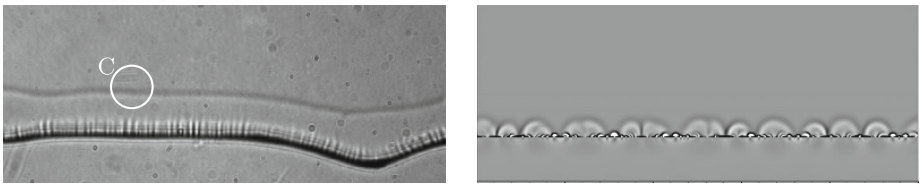

(a) Experiment horizontal (b) Simulation G=0

Fig. 8. *Thick, horizontal HS cell*: shadowgraph images at t = 1.1 for (a) experiment with $2\epsilon = 1$ mm and (b) simulation with $G = 0$, $\gamma = 1600$. White circle with C mark (a) illustrates the solute front observed in experiment.

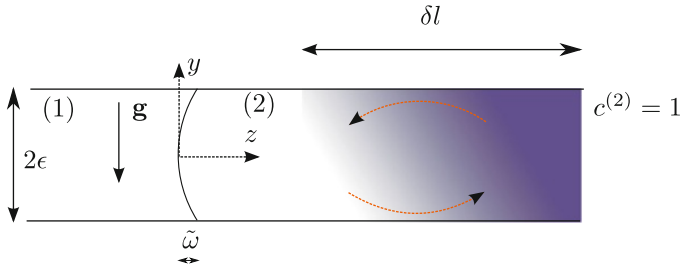

Fig. 9. Sketch of horizontal HS cell to illustrate density-gradient driven convection.

(adjacent to the interface) lies next to lighter unmixed fluid situated further away from the interface (dark color in Fig. 9).

Since gravity ($\mathbf{g}$) acts perpendicular (in -$\mathbf{e}_y$-direction for horizontal orientation) to the density gradient, a flow ($u_y \neq 0$) is inevitably established due to the horizontal pressure gradient $\partial_z p$. The present 2D model is not able to capture such a flow across the gap, but we discuss how its amplitude can roughly be estimated by the so called Hadley flow (cf. [24] p. 80).

This Hadley flow is pictured as follows: Consider a fluid layer infinitely extended in z-direction $-\infty < \tilde{z} < +\infty$ which is bounded in $\tilde{y}$ direction by solid walls at $\tilde{y} = \epsilon, -\epsilon$ with a constant solute gradient $\partial_{\tilde{z}}\tilde{c}$ of magnitude $\Delta\tilde{c}/\delta l$. This well-known problem has a time-independent solution [24]. The dimensional velocity $\tilde{U}$ established in the z-direction with material properties of layer (2) reads

$$\tilde{U}(\tilde{y}) = -\frac{g\beta_c^{(2)}(2\epsilon)^3}{\nu^{(2)}6}\frac{\Delta\tilde{c}}{\delta l}\left[\left(\frac{\tilde{y}}{2\epsilon}\right)^3 - \frac{\tilde{y}}{2\epsilon}\frac{1}{4}\right]. \tag{15}$$

In order to apply this simple model to the experimental situation, we estimate the solute difference $\Delta\tilde{c}$ in phase (2) by the difference between the initial concentration c_0 and the concentration at the interface for a semi-infinite system undergoing only pure diffusion [38], i.e. $\Delta\tilde{c} = c_0 - c_0/(1 + H^{-1}D^{-0.5}) \approx 0.0794c_0$. The selection of an appropriate length δl on which concentration gradients exist is a delicate task as our flow is not infinitely extended. For simplicity, we assume a distance of $\delta l = 0.1d^{(1)}$, which is approximately the vertical extent of the convective structures (a more sophisticated approach can be found in [25]). Finally, a characteristic nondimensional velocity U is taken at $\tilde{y} = \epsilon/2$ (with material parameters tabulated in Table 1). For 0.5 mm (1 mm) plate distance this amounts to $U = 0.0033$ ($U = 0.027$).

Consequently, a buoyancy-driven convection explains the appearance of a solute front for the thick and horizontal cell in Fig. 8a. This interpretation is supported by three facts. First, the estimated value U=0.027 is of similar order as the measured

speed of ≈0.04, corresponding to the dashed line in Fig. 6b. Second, no solute front is visible in the thin cell, which is in line with the small velocity (U=0.0033) predicted. Third, the propagation of the solute front in the thick cell bears a strong resemblance with that of an $A+B \rightarrow C$ *reaction front* [2,10] for which the buoyancy-driven origin was clearly proved in [2]. Moreover, in interference with the buoyant convection, the fine Marangoni-driven solute structures at the interface seem to be drawn towards the solute front as visible in Fig. 8a. These flow characteristics were also observed in a similar setup of chemo-Marangoni convection (Fig. 6a in [2]).

5 Discussion and conclusion

The major findings of the preceding sections can be summarized as follows:

- Thin, vertical HS cell: Marangoni roll cells without internal substructure develop. The experimental flow structures are qualitatively well represented by the simulated Marangoni roll cells.
- Thick, vertical HS cell: Reduced wall friction causes increased mass transfer and substructured roll cells which are comparable to the ones formerly seen in a 3D setup [16,23]. In experiments, cell height growth is also enhanced with increased gap width, but the substructures are only faintly visible.
- Thin, horizontal HS cell: In simulations with zero Grashof number, the suppression of stabilizing density stratification leads to an increased mass transfer. This enhanced cell height growth is also observed in experiment.
- Thick, horizontal HS cell: In the experiment, a propagating solute front appears which is not explained by our gap-averaged model.
- In general, experiments appear accelerated in time compared to simulations.

The observed differences can be explained by the limitations of the 2D model and the experimental filling procedure. The most obvious limitations are *3D flow effects*, i.e. a variation of concentration across the gap and deviations from the parabolic velocity profile. In detail, three features that lead to 3D effects might be noted. Firstly, the Marangoni roll cells which occur in the simulations are smaller than the gap size. By this, it is expected that Marangoni roll cells are also amplified across the gap ($\partial_y c \neq 0$). Secondly, the circular meniscus[2] might lead to flow from the three phase contact line to the meniscus apex, since the meniscus apex reaches further into the water-rich phase. Thirdly, for horizontal orientation, a density instability is induced, which leads to a buoyancy-driven flow across the gap ($u_y \neq 0$). Although its impact is not that obvious for the small gap width, a certain influence of this additional transport mechanism on the pattern growth can be assumed here as well.

Besides the 3D flow effects, deviations from the assumed plane interface are another source of discrepancies between experimental and numerical results. Apart from the circular meniscus, the position of the interface $\xi(x, y)$ also changes in lateral direction ($\partial_x \xi(x, y) \neq 0$) as a result of the filling procedure. This imposes a higher concentration at parts reaching deeper into the delivering phase. Furthermore, the interfacial area increases by 10–15% due to interfacial deformations (circular meniscus and lateral undulation).

In spite of the limitations of our theoretical and experimental approach, the qualitative agreement of our results for the vertical orientation and the small gap width show promising options for a quantitative analysis of solutal Marangoni convection. However, we can also conclude that the HS model is expected to be more precise for systems where large Marangoni cells without substructure develop, e.g. in [3], since

[2] The interface position $z = \xi(x, y)$ has a circular shape for fixed x.

3D flow effects will be less pronounced in that case. These limitations similarly concern 2D simulations without the influence of wall friction. Hence our study likewise provides some guidance for their validity.

A further option to check the applicability of the 2D model to an experiment might be deduced from the scale invariance noted in [16]. In the 3D setup of [16], a change in the initial concentration c_0 is equivalent to the change of length $L \sim c_0^{-1}$ and timescale $T \sim c_0^{-2}$. The HS model includes an additional outer length, i.e. the plate distance 2ϵ, which also needs to be scaled $2\epsilon \sim c_0^{-1}$. For instance, by doubling the plate distance and halving the concentration in experiment, the pattern remains unchanged if the 2D model is applicable. However, we note that the requirement of negligible interfacial deformations still holds for this comparison.

Financial support by the Deutsche Forschungsgemeinschaft in the framework of Priority Program 1506 is gratefully acknowledged. Computing center of TU Ilmenau is acknowledged for computing resources, and Prof. H. Linde for numerous fruitful discussions.

References

1. M. Budroni, L. Riolfo, L. Lemaigre, F. Rossi, M. Rustici, A. De Wit, J. Phys. Chem. Lett. **5**, 875 (2014)
2. K. Eckert, L. Rongy, A. De Wit, Phys. Chem. Chem. Phys. **14**, 7337 (2012)
3. K. Eckert, M. Acker, R. Tadmouri, V. Pimienta, J. Nonlin. Sci. **22**, 037112(10) (2012)
4. K. Kostarev, A. Shmyrov, A. Zuev, A. Viviani, Exp. Fluids **51**, 457 (2011)
5. A. Heinze, K. Eckert, M.J. Hauser, S. Odenbach, Acta Astronaut. **68**, 707 (2011)
6. A. Grahn, Chem. Eng. Sci. **61**, 3586 (2006)
7. D. Bratsun, A. De Wit, Phys. Fluids **16**, 1082 (2004)
8. S. Backhaus, K. Turitsyn, R. Ecke, Phys. Rev. Lett. **106**, 104501 (2011)
9. K. Schwarzenberger, K. Eckert, S. Odenbach, Chem. Eng. Sci. **68**, 530 (2012)
10. Y. Shi, K. Eckert, Chem. Eng. Sci. **61**, 5523 (2006)
11. K. Eckert, M. Acker, Y. Shi, Phys. Fluids **16**, 385 (2004)
12. H. Linde, S. Pfaff, C. Zirkel, Z. Phys. Chem. **225**, 72 (1964)
13. Y. Sha, H. Chen, Y. Yin, S. Tu, L. Ye, Y. Zheng, Ind. Eng. Chem. Res. **49**, 8770 (2010)
14. R. Birikh, A. Zuev, K. Kostarev, R. Rudakov, Fluid Dyn. **41**, 514 (2006)
15. C.V. Sternling, L.E. Scriven, AIChE J. **5**, 514 (1959)
16. T. Köllner, K. Schwarzenberger, K. Eckert, T. Boeck, Phys. Fluids **25**, 092109 (2013)
17. E. Schwarz, Ph.D. thesis, HU Berlin, 1967
18. Y. Shi, K. Eckert, Chem. Eng. Sci. **63**, 3560 (2008)
19. W. Boos, A. Thess, J. Fluid Mech. **352**, 305 (1997)
20. D.A. Bratsun, A. De Wit, Chem. Eng. Sci. **66**, 5723 (2011)
21. T. Boeck, A. Nepomnyashchy, I. Simanovskii, A. Golovin, L. Braverman, A. Thess, Phys. Fluids **14**, 3899 (2002)
22. W. Merzkirch, *Flow Visualization* (Academic Press, 1987)
23. K. Schwarzenberger, T. Köllner, H. Linde, T. Boeck, S. Odenbach, K. Eckert, Adv. Coll. Interface Sci. **206**, 344 (2014)
24. M. Lappa, *Thermal Convection: Patterns, Evolution and Stability* (John Wiley & Sons, 2009)
25. J. Patterson, J. Imberger, J. Fluid Mech. **100**, 65 (1980)
26. A. Nepomnyashchy, I. Simanovskii, J.C. Legros, *Interfacial Convection in Multilayer Systems* (Springer, 2011)
27. G. Taylor, Proc. R. Soc. Lond. Ser. A: Math. Phys. Sci. **219**, 186 (1953)
28. R. Aris, Proc. R. Soc. Lond. Ser. A: Math. Phys. Sci. **235**, 67 (1956)
29. M. Leconte, J. Martin, N. Rakotomalala, D. Salin, Y.C. Yortsos, J. Chem. Phys. **120**, 7314 (2004)

30. N. Jarrige, I. Bou Malham, J. Martin, N. Rakotomalala, D. Salin, L. Talon, Phys. Rev. E **81**, 066311 (2010)
31. W.B. Zimmerman, G.M. Homsy, Phys. Fluids **8**, 1859 (1991)
32. C. Ruyer-Quil, Comptes Rendus de l'Académie des Sciences-Series IIB-Mechanics **329**, 337 (2001)
33. J. Martin, N. Rakotomalala, D. Salin, Phys. Fluids **14**, 902 (2002)
34. F. Gallaire, P. Meliga, P. Laure, C.N. Baroud, Phys. Fluids **26**, 062105 (2014)
35. J. Zeng, Y.C. Yortsos, D. Salin, Phys. Fluids **15**, 3829 (2003)
36. R.N. Horne, F. Rodriguez, Geophys. Res. Lett. **10**, 289 (1983)
37. P. Petitjeans, C. Chen, E. Meiburg, T. Maxworthy, Phys. Fluids **11**, 1705 (1999)
38. J. Crank, *The Mathematics of Diffusion* (Clarendon Press Oxford, 1975)